


Geometric Ramsey interferometry with a tripod scheme

Chetan Sriram Madasu^{1,2,3,*}, Ketan Damji Rathod^{3,†}, Chang Chi Kwong^{1,2} and David Wilkowski^{1,2,3}

¹*Nanyang Quantum Hub, School of Physical and Mathematical Sciences, Nanyang Technological University, 21 Nanyang Link, Singapore 637371, Singapore*

²*MajuLab, International Joint Research Unit IRL 3654, CNRS, Université Côte d'Azur, Sorbonne Université, National University of Singapore, Nanyang Technological University, Singapore*

³*Center for Quantum Technologies, National University of Singapore, Singapore 117543, Singapore*

 (Received 16 September 2023; revised 13 March 2024; accepted 10 April 2024; published 8 May 2024)

Ramsey interferometry is a key technique for precision spectroscopy and for probing the coherence of quantum systems. Typically, an interferometer is constructed using two quantum states and involves a time-dependent interaction with two short resonant electromagnetic pulses. Here, we explore a different type of Ramsey interferometer where we perform quantum state manipulations by geometrical means, eliminating the temporal dependence of the interaction. We use a resonant tripod scheme in ultracold strontium atoms where the interferometric operation is restricted to a two-dimensional dark-state subspace in the dressed-state picture. The observed interferometric phase accumulation is due to an effective geometric scalar term in the dark-state subspace, which remarkably does not vanish during the free evolution time when the light-matter interaction is turned off. This study opens the door for more robust interferometers operating on multiple input-output ports.

DOI: [10.1103/PhysRevApplied.21.L051001](https://doi.org/10.1103/PhysRevApplied.21.L051001)

Ramsey interferometry employs temporally separated electromagnetic pulses to probe the energy difference and the coherence between two quantum states [1,2]. Whether employing internal, external, or both states of atoms, Ramsey interferometers have become essential tools to probe quantum states in quantum simulations [3,4], in quantum computing [5], in interband spectroscopy [6], and in atomic clocks at or below the quantum projection noise limit [7,8], to name a few.

In contrast to the majority of Ramsey interferometers that rely on the dynamical evolution of the system mediated through light-matter interaction, we explore here a geometric Ramsey interferometer governed by adiabatic evolution in the degenerate dark-state subspace of a tripod scheme. We find that the phase accumulation during the free evolution time arises from a geometric scalar potential. Surprisingly, this potential retains its physical significance even when the pulses are turned off as long as the dressed states of interest remain adiabatically connected to the bare states. Geometric scalar potentials are at the origin of the so-called dark optical lattices [9–11],

and have been employed to create subwavelength barriers in an effective spin [12] or spinless [13] configuration. Though the geometric scalar potential plays a role in shaping periodic potential, it is essentially overlooked in the bulk because of the moderate strength in comparison with commonly used optical potentials [14,15].

The interferometer operates on an ultracold gas of ^{87}Sr atoms. The gas is prepared using a two-stage magneto-optical trap [16,17], followed by evaporative cooling in a crossed-beam optical-dipole trap [18]. We then obtain a quantum degenerate Fermi gas comprised of $N = 4.5(2) \times 10^4$ atoms in the $m_F = 9/2$ stretched Zeeman substate at a temperature of $T_0 = 50(3)$ nK. This temperature corresponds to $T_0/T_F = 0.25(2)$, where T_F is the Fermi temperature. Additionally, $T_0/T_R = 0.21(2)$, where T_R is the recoil temperature associated with the tripod transitions. After evaporative cooling, the optical trap is switched off, and a magnetic field bias is turned on to isolate a tripod scheme on the $^1S_0, F_g = 9/2 \rightarrow ^3P_1, F_e = 9/2$ hyperfine multiplet of the intercombination line at 689 nm [19]. Three laser beams resonantly couple the three internal ground states $|a\rangle \equiv |F_g, m_F\rangle$, with $a = \{1, 2, 3\}$ and $m_F = \{5/2, 7/2, 9/2\}$, respectively, to a common excited state $|e\rangle \equiv |F_e, m_F = 7/2\rangle$, as shown in Figs. 1(a) and 1(b). The light-matter interaction is characterized by three complex Rabi frequencies Ω_a , associated with the $|a\rangle \rightarrow |e\rangle$ transitions.

*Corresponding author: chetansr001@e.ntu.edu.sg

†Present address: Bennett University, Greater Noida 201310, India.

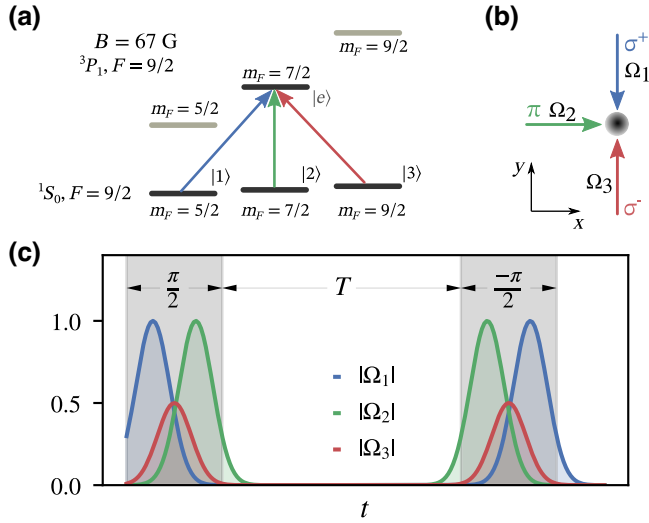


FIG. 1. Schematic showing the implementation of the geometric Ramsey interferometry pulse sequence. (a) Energy levels of ^{87}Sr atoms involved in the tripod scheme. A bias magnetic field of 67 G shifts adjacent excited magnetic states by approximately 930Γ , where $\Gamma/2\pi = 7.5$ kHz is the linewidth of the intercombination line. (b) The spatial configuration of the tripod beams. (c) Relative Rabi frequencies of the tripod beams as a function of time. The Gaussian pulses are parameterized as $|\Omega_a(t)| = |\Omega_{0a}|e^{-(t-t_a^{(j)})^2/4\sigma_t^2}$, where $|\Omega_{0a}|$ is the peak Rabi frequency with $a = 1, 2, 3$, $\sqrt{2}\sigma_t$ is the temporal standard deviation, and $t_a^{(j)}$ are the centers of the Gaussian pulses for the $\pi/2$ pulse ($j = 1$) and $-\pi/2$ pulse ($j = 2$). The pulse sequence corresponds to $t_1^{(j)} = t_3^{(j)} - \eta\sigma_t$, $t_2^{(j)} = t_3^{(j)} + \eta\sigma_t$, $t_3^{(1)} = 4\sigma_t$, and $t_3^{(2)} = t_3^{(1)} + 8\sigma_t + T$, with $|\Omega_{01}| = |\Omega_{02}| = 2|\Omega_{03}| \approx 2\pi \times 260$ kHz and η is the separation parameter with a value of 1.8. Here, the length of $\pi/2$ pulses is defined as the duration of the σ^- Gaussian pulse, i.e., $8\sigma_t$. Therefore, the separation between two $\pi/2$ pulses, T , is defined as the free evolution time.

Our geometric Ramsey interferometric sequence consists of a $\pi/2$ pulse and a $-\pi/2$ pulse, temporally separated by a free evolution time T as sketched in Fig. 1(c). The first $\pi/2$ pulse, composed of three Gaussian pulses, puts the atoms initially in the $|3\rangle$ state into a coherent superposition of $|3\rangle$ and $|1\rangle$ states, ideally with equal probabilities. The relative population of the output states does not depend on the pulse duration, due to its geometrical nature. It is instead controlled by the relative peak Rabi frequency amplitude $|\Omega_{03}|$ of beam 3 with respect to the peak Rabi frequency amplitudes of beams 1 and 2, which are set equal, namely $|\Omega_{01}| = |\Omega_{02}|$ [21]. The second pulse, closing the interferometer, is a $-\pi/2$ pulse, meaning that, without any further phase accumulation, the second pulse brings back the atom into its initial state, namely $|3\rangle$. Here, an extra phase accumulation between the two arms occurs reducing the population of $|3\rangle$ at the interferometer output, as shown in Fig. 2 (red squares). Importantly, we note that the remaining population, instead of going to the state $|1\rangle$

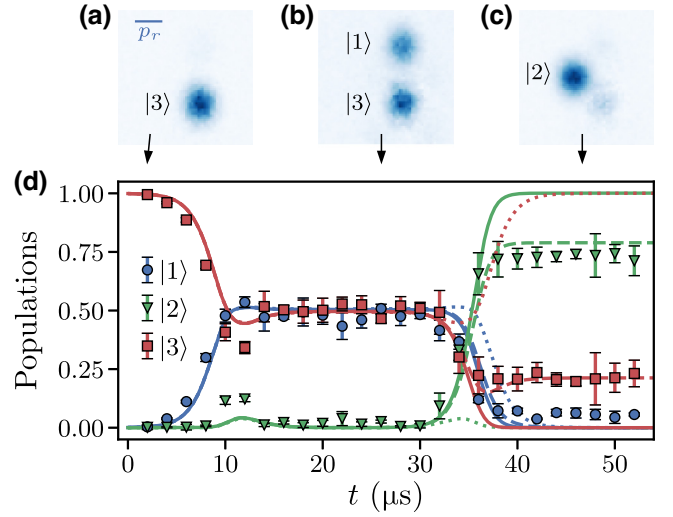


FIG. 2. (a)–(c) Fluorescence images of the ultracold gas after 9 ms of time of flight; see Ref. [20] for more details. The images are taken before the first pulse ($t = 0$), during the free evolution time ($t = 18 \mu\text{s}$), and after the second pulse ($t = 48 \mu\text{s}$), respectively. Each peak in the momentum distribution is associated with a bare state as indicated in each panel. We extract the bare state populations by fitting each peak to a two-dimensional (2D) Gaussian distribution. (d) Populations of the bare states during the interferometric sequence, with $\sigma_t = 2.5 \mu\text{s}$ and $T = 6 \mu\text{s}$. The experimental data points are plotted with markers with the error bars representing one standard deviation confidence. The solid and dashed curves represent the numerical integration of Eq. (4) (see Ref. [20] for more details) for temperatures of 0 and 50 nK, respectively. The dotted curve represents the zero temperature theoretical expectations, without the scalar term \hat{Q} .

(blue circles) as expected for a standard two-level Ramsey interferometer, is now transferred to state $|2\rangle$ (green triangles). This unusual behavior originates from the order of the Gaussian pulses acting on the tripod scheme. As shown in Fig. 1(c), the second pulse sequence is a temporal mirror image of the first one, so the beam 1 pulse, which is finishing the sequence, prevents population in state $|1\rangle$ as expected for any STIRAP scheme [22].

To confirm the phase-sensitive nature of the experiment, we purposely apply a phase jump Φ to the beam 3 at the center of the free evolution sequence when the laser is considered to be turned off. As expected, the interferometric readout from the atomic bare state populations after the second pulse shows a sinusoidal evolution as a function of the introduced phase jump [see Fig. 3(a)]. We note that a phase jump of $\Phi = \pi$ rotates the interferometer output fringe by half a period.

During the free evolution time T , a phase accumulation occurs, which has a simple physical origin in the bare-state picture. The coherent transfer between the state $|3\rangle$ and the state $|1\rangle$ redistributes a photon between the beams 3 and 1, which leads to a momentum kick of $2p_r\hat{y}$ on the atom,

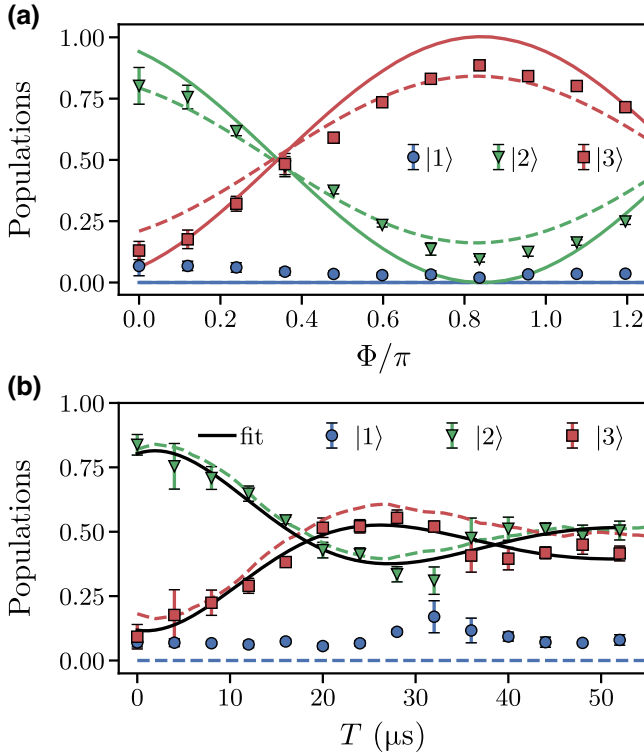


FIG. 3. (a) Interference fringes generated with an abrupt phase change of the beam 3 coupling the $|3\rangle \rightarrow |e\rangle$ transition. This phase jump Φ is introduced at the middle of the free evolution time, $T = 6 \mu\text{s}$. The solid and dashed curves represent the numerical integration for temperatures of 0 and 50 nK, respectively. (b) Populations of bare states after the Ramsey pulse sequence as a function of free evolution time T . The black solid curves represent a fit using an exponentially damped oscillation. The colored dashed curves are the predictions of the adiabatic model; see Ref. [20] for more details.

as shown in Fig. 2(b). Here, $p_r = \hbar k$ is the recoil momentum associated with a $\lambda = 689\text{-nm}$ photon, \hbar is the reduced Planck constant, and $k = 2\pi/\lambda$ is the wave number of the light field. Therefore, the phase accumulation corresponds to $\Delta E_k T/\hbar$, where $\Delta E_k = 2p_r^2/m$ is the kinetic energy difference between the two bare states and m is the atomic mass. We fit the Ramsey interferometer output evolution as a function of T with a damped oscillation and find an angular frequency of $2\pi \times 19.8(16)$ kHz [see black solid curves in Fig. 3(b)], in agreement with the theoretical prediction of $\Delta E_k/\hbar = 2\pi \times 19.2$ kHz.

At finite temperature, the oscillation is damped due to the momentum dispersion of the gas. In Fig. 3(b), we observe a good agreement of the experiment with an adiabatic model at a temperature $T_0 = 50$ nK (see colored dashed curves), indicating that the temperature is the dominant dephasing mechanism limiting the experimental coherence time. Deviations from the model prediction are mainly due to a residual diabatic contribution; for more detail, see Ref. [20]. The damping time, extracted from

the fit, is found to be $\tau = 23(4) \mu\text{s}$. Since $\tau \Delta E_k/\hbar \gtrsim 1$, only a few oscillations are visible, limiting the sensitivity of the frequency measurement. The coherence time can be improved either by reducing the temperature using for example delta-kick cooling [23] or by post-selection of a narrow momentum window after a long time of flight [24]. Alternatively, Mach-Zehnder or Ramsey-Bordé types of interferometric pulse sequence can be in principle implemented to limit the dephasing due to temperature.

A rigorous theoretical treatment of the geometric Ramsey interferometer can be done with a brute-force diagonalization of the time-dependent Hamiltonian of the system. However, physical interpretation together with significant simplifications are possible by changing the original bare-state basis to the dressed-state basis of the internal Hamiltonian, defined by two long-lived zero-energy dark states, namely

$$\begin{aligned} |D_1(\mathbf{r}, t)\rangle &= \sin \varphi(t) e^{2iky} |1\rangle - \cos \varphi(t) e^{ik(y-x)} |2\rangle, \\ |D_2(\mathbf{r}, t)\rangle &= \cos \vartheta(t) (\cos \varphi(t) e^{2iky} |1\rangle + \sin \varphi(t) e^{ik(y-x)} |2\rangle) \\ &\quad - \sin \vartheta(t) |3\rangle, \end{aligned} \quad (1)$$

and two bright states that contain the bare excited state, so subject to a fast decay by photon spontaneous emission. Moreover, the bright states are light shifted by $\pm \hbar\Omega$, where $\vartheta = \cos^{-1}(|\Omega_3|/\Omega)$, $\varphi = \tan^{-1}(|\Omega_2|/|\Omega_1|)$, and $\Omega = \sqrt{|\Omega_1|^2 + |\Omega_2|^2 + |\Omega_3|^2}$ [14].

A first simplification occurs because the internal state evolution can be restricted to the dark-state subspace. Indeed, the bright-state light shift corresponds to the highest energy scale of the problem ($\Omega \simeq 2\pi \times 410$ kHz), and the initial bare state $|3\rangle$ is adiabatically connected to $|D_2\rangle$ [25]. Overall, the populations of the bright states remain negligible during the Ramsey sequence. This point is experimentally checked noticing that there is no significant heating of the gas after the Ramsey sequence (for more details, see Ref. [20]). Limiting ourselves now to the dark-state subspace, the effective Hamiltonian reads [25,26]

$$\hat{H} = \frac{\hat{\mathbf{p}}^2 \otimes \mathbb{1}}{2m} - \frac{\hat{\mathbf{A}} \cdot \hat{\mathbf{p}}}{m} + \hat{Q} + \hat{w}, \quad (2)$$

where $\mathbb{1}$ is a two-dimensional identity operator defined in the dark-state subspace and the operators $\hat{\mathbf{A}}$, \hat{Q} , and \hat{w} have the respective matrix entries

$$\begin{aligned} \mathbf{A}_{\mu\nu} &= i\hbar \langle D_\mu | \nabla D_\nu \rangle, \\ \mathbf{Q}_{\mu\nu} &= \frac{\hbar^2}{2m} \langle \nabla D_\mu | \nabla D_\nu \rangle, \\ w_{\mu\nu} &= -i\hbar \langle D_\mu | \frac{\partial}{\partial t} D_\nu \rangle. \end{aligned} \quad (3)$$

Since $|\nabla| \sim k$ and the size of the momentum distribution is smaller than the recoil momentum p_r , as a second simplification, we neglect the kinetic and spin-orbit coupling contributions with respect to the scalar term \hat{Q} , i.e., the first and second right-hand-side terms of the Hamiltonian in Eq. (2), respectively. The state evolution in the dark-state subspace is then given by the unitary transformation

$$\hat{U}(t) = \mathcal{T} \exp \left[-i \int_0^t \left(\hat{Q}(t') + \hat{w}(t') \right) dt' \right], \quad (4)$$

where \mathcal{T} is the time-ordering operator. From the spatial configuration of our tripod beams [see Fig. 1(b)], we derive the following expression for the scalar term:

$$\hat{Q} = -\frac{p_r^2}{2m} \begin{pmatrix} 2(1 + \sin^2 \varphi) & \cos \vartheta \sin 2\varphi \\ \cos \vartheta \sin 2\varphi & 2 \cos^2 \vartheta (1 + \cos^2 \varphi) \end{pmatrix} \quad (5)$$

and the final term on the right-hand side of Eq. (2) reads

$$\hat{w} = \hbar \cos \vartheta \frac{\partial \varphi}{\partial t} \hat{\sigma}_y, \quad (6)$$

where $\hat{\sigma}_y$ is the y -component Pauli matrix. The operator \hat{w} plays a key role since it is responsible for the geometric atomic beam splitting [15,21,27]. We also note that this term has no specific energy scale since it depends on the temporal profile of the Gaussian pulse. The latter has to be slow enough to fulfill the adiabatic condition, namely $\langle \hat{w} \rangle \ll \hbar \Omega$, at all times.

The solid curves in Figs. 2(d) and 3 are obtained through numerical integrations of Eq. (4), whereas the projections onto the bare states are extracted from Eq. (1). The dashed curves are obtained by averaging over the momentum distribution of our thermal sample, with a temperature of $T_0 = 50$ nK. Here the momentum dependence is obtained in the semiclassical limit by reintroducing the previously overlooked first and second terms on the right-hand side of Eq. (2); see main text and Ref. [20] for more details.

Our model, together with the damping due to the finite temperature, captures the main experimental features well, opening the door for insightful physical interpretations of this geometric Ramsey interferometer. As we have already mentioned, the initial state $|3\rangle$ is connected to $|D_2\rangle$ dark state [25]. For a complete description, we shall highlight that the dark states at the end of the $\pi/2$ pulse are asymptotically connected to the bare states as $|D_1\rangle \rightarrow |1\rangle$ and $|D_2\rangle \rightarrow |3\rangle$ [21]. This point can be easily verified, using Eq. (1) and noticing that at the end of the $\pi/2$ pulse $\varphi \rightarrow \pi/2$ and $\vartheta \rightarrow \pi/2$. Similarly, at the end of the $-\pi/2$ pulse, the dark states are connected to the bare states as $|D_1\rangle \rightarrow |2\rangle$ and $|D_2\rangle \rightarrow |3\rangle$. Hence, we understand that even if the geometric Ramsey interferometer is fundamentally a two-level interferometer in the dark-state subspace, we still

need the three bare-ground states for a complete description. It leads to a multiple input-output port device, where the matter-wave propagation direction can be controlled by the pulse ordering sequence and a phase-sensitive signal [compare the bare-state population distribution locations in Figs. 2(a)–2(c)]. This principle can be utilized for implementing an atomtronic bilateral switch where either the phase jump Φ or the free evolution time T can be used as the switching control parameter.

Another insightful interpretation of our model concerns the nature of the phase accumulation during the free evolution time, which can be clearly associated with the scalar term \hat{Q} . Indeed, during the free evolution time $\partial \varphi / \partial t \rightarrow 0$, so $w_{\mu\nu} \rightarrow 0$. The last remaining term, which is the scalar potential, takes the asymptotic expression

$$\lim_{\varphi \rightarrow \pi/2, \vartheta \rightarrow \pi/2} \hat{Q} = -\frac{p_r^2}{m} \begin{pmatrix} 2 & 0 \\ 0 & 0 \end{pmatrix}. \quad (7)$$

Moreover, the dotted curves in Fig. 2(d) correspond to numerical integrations of Eq. (4) setting $\hat{Q} = \hat{Q}$ at all times. Here, no phase shift is observed as the population transfers back to $|3\rangle$ at the output of the interferometer. A similar situation occurs with trapped ions in the Lamb-Dicke regime [15]. We note that the presence of a nonzero \hat{Q} term leads to a nonintuitive situation where the dressed-state picture remains meaningful even if the tripod beams are turned off, provided that the adiabatic asymptotic connection, depicted by Eq. (7), is fulfilled. In addition, the energy difference between the states $|D_1\rangle$ and $|D_2\rangle$ leads to a phase accumulation during the free evolution time of $|\hat{Q}_{11} - \hat{Q}_{22}|T/\hbar = 2p_r^2 T/\hbar m$ in agreement with the previously discussed bare-state approach.

Finally, we check the geometrical nature of the matter-wave splitter, searching for time-independent behavior by either compressing or inflating the temporal sequence of the matter-wave splitter. For instance, the first $\pi/2$ pulse will rotate the initial $|D_2\rangle \equiv |3\rangle$ by a polar angle $\theta = \pi/2$ into the equatorial plane in the Bloch sphere representation. We show in Fig. 4 the deviation $\Delta\theta = \theta_{\text{exp}} - \pi/2$ of the experimentally measured polar angle θ_{exp} as a function of the temporal standard deviation of the Gaussian pulses σ_t . When the duration of the pulse sequence is within $3 \mu\text{s} < \sigma_t < 15 \mu\text{s}$, the deviation is in agreement with a null value, indicating a time-independent geometric matter-wave splitter. For $\sigma_t < 3 \mu\text{s}$, the nonzero deviation indicates that the pulse sequence is not fully adiabatic. For $\sigma_t > 15 \mu\text{s}$, the adiabatic approximation is fulfilled, but \hat{w} becomes too small with respect to the spin-orbit and kinetic terms of Eq. (2), leading to a breakdown of the approximation of our model given by Eq. (4) [21]. We use $\sigma_t = 2.5 \mu\text{s}$ in the experiment in order to reduce the length of the pulse sequence as a trade-off between nonadiabaticity and effects of thermal dispersion. Under this condition, we check that

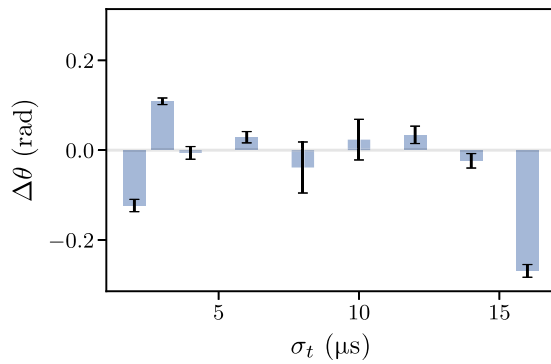


FIG. 4. Deviation of the polar angle of the dark-state coherent superposition after the first $\pi/2$ pulse as a function of σ_t .

the spontaneous emission is weak, which is a good indication that the adiabatic approximation remains correct; for more details, see Ref. [20].

In conclusion, we have explored a geometric Ramsey interferometer based on a tripod scheme. This interferometer reduces to a two-level system in the dark-state subspace but can also be viewed as connecting the three internal ground-bare states in a configuration with multiple input-output ports. We show that the phase accumulation during the free-evolution time is due to a geometric scalar potential that encapsulates the kinetic energy difference of the bare states. Because these states are time independent, geometric manipulations of quantum states are generally more robust than their dynamical counterparts. This robustness can be translated here to an interferometer that is insensitive to the mean velocity of the atomic ensemble, making it suitable for possible applications in quantum simulations and computing, and atomtronics circuits [13,28–31].

In the future, other types of interferometers, such as Ramsey-Bordé interferometers [32,33] or Mach-Zehnder interferometers [34], can be envisioned using similar geometric approaches. The former can be utilized for precision measurements of the photon recoil shift to determine the fine-structure constant [35,36], while the latter can serve for inertial sensing applications such as gravimetry [37], gradiometry [38], or tests of the equivalence principle [39], to name a few. Finally, the inherent slow response time of adiabatic transformation can be addressed using shortcuts to adiabaticity schemes [40], enabling the implementation of large-area interferometers [41].

Acknowledgements. The authors thank Du Jinyi and Lucas Gabardos for careful reading of the manuscript. This work was supported by the CQT/MoE (Grant No. R-710-002-016-271), the Singapore Ministry of Education Academic Research Fund Tier2 (Grant No. MOE-T2EP50220-0008), and the Temasek Laboratories (Grant No. TLSP23-08).

- [1] N. F. Ramsey, A new molecular beam resonance method, *Phys. Rev.* **76**, 996 (1949).
- [2] N. Ramsey, in *International Series of Monographs on Physics* (OUP Oxford, Oxford, United Kingdom, 1985).
- [3] M. Cetina, M. Jag, R. S. Lous, I. Fritsche, J. T. M. Walraven, R. Grimm, J. Levinsen, M. M. Parish, R. Schmidt, M. Knap, and E. Demler, Ultrafast many-body interferometry of impurities coupled to a Fermi sea, *Science* **354**, 96 (2016).
- [4] T. Li, L. Duca, M. Reitter, F. Grusdt, E. Demler, M. Endres, M. Schleier-Smith, I. Bloch, and U. Schneider, Bloch state tomography using Wilson lines, *Science* **352**, 1094 (2016).
- [5] P. J. Lee, K.-A. Brickman, L. Deslauriers, P. C. Haljan, L.-M. Duan, and C. Monroe, Phase control of trapped ion quantum gates, *J. Opt. B: Quantum Semiclass. Opt.* **7**, S371 (2005).
- [6] D. Hu, L. Niu, S. Jin, X. Chen, G. Dong, J. Schmiedmayer, and X. Zhou, Ramsey interferometry with trapped motional quantum states, *Commun. Phys.* **1**, 29 (2018).
- [7] G. Santarelli, P. Laurent, P. Lemonde, A. Clairon, A. G. Mann, S. Chang, A. N. Luiten, and C. Salomon, Quantum projection noise in an atomic fountain: A high stability cesium frequency standard, *Phys. Rev. Lett.* **82**, 4619 (1999).
- [8] E. Pedrozo-Peñañiel, S. Colombo, C. Shu, A. F. Adiyatullin, Z. Li, E. Mendez, B. Braverman, A. Kawasaki, D. Akamatsu, Y. Xiao, and V. Vuletić, Entanglement on an optical atomic-clock transition, *Nature* **588**, 414 (2020).
- [9] R. Dum and M. Olshanii, Gauge structures in atom-laser interaction: Bloch oscillations in a dark lattice, *Phys. Rev. Lett.* **76**, 1788 (1996).
- [10] S. K. Dutta, B. K. Teo, and G. Raithel, Tunneling dynamics and gauge potentials in optical lattices, *Phys. Rev. Lett.* **83**, 1934 (1999).
- [11] R. P. Anderson, D. Trypogeorgos, A. Valdés-Curiel, Q.-Y. Liang, J. Tao, M. Zhao, T. Andrijauskas, G. Juzeliūnas, and I. B. Spielman, Realization of a deeply subwavelength adiabatic optical lattice, *Phys. Rev. Res.* **2**, 013149 (2020).
- [12] E. Gvozdiavas, P. Rackauskas, and G. Juzeliūnas, Optical lattice with spin-dependent sub-wavelength barriers, *SciPost Phys.* **11**, 100 (2021).
- [13] Y. Wang, S. Subhankar, P. Bienias, M. Lacki, T.-C. Tsui, M. A. Baranov, A. V. Gorshkov, P. Zoller, J. V. Porto, and S. L. Rolston, Dark state optical lattice with a subwavelength spatial structure, *Phys. Rev. Lett.* **120**, 083601 (2018).
- [14] J. Dalibard, F. Gerbier, G. Juzeliūnas, and P. Öhberg, Colloquium: Artificial gauge potentials for neutral atoms, *Rev. Mod. Phys.* **83**, 1523 (2011).
- [15] K. Toyoda, K. Uchida, A. Noguchi, S. Haze, and S. Urabe, Realization of holonomic single-qubit operations, *Phys. Rev. A* **87**, 052307 (2013).
- [16] T. Chaneliere, L. He, R. Kaiser, and D. Wilkowski, Three dimensional cooling and trapping with a narrow line, *Eur. Phys. J. D* **46**, 507 (2008).
- [17] T. Yang, K. Pandey, M. S. Pramod, F. Leroux, C. C. Kwong, E. Hajiyeve, Z. Y. Chia, B. Fang, and D. Wilkowski, A high flux source of cold strontium atoms, *Eur. Phys. J. D* **69**, 226 (2015).
- [18] M. Hasan, C. S. Madasu, K. D. Rathod, C. C. Kwong, C. Miniatura, F. Chevy, and D. Wilkowski, Wave packet

- dynamics in synthetic non-Abelian gauge fields, *Phys. Rev. Lett.* **129**, 130402 (2022).
- [19] M. Hasan, C. Madasu, K. Rathod, C. Kwong, and D. Wilkowski, Evolution of an ultracold gas in a non-Abelian gauge field: Finite temperature effect, *Quantum. Elec. (Woodbury)* **52**, 532 (2022).
- [20] See Supplemental Material at <http://link.aps.org/supplemental/10.1103/PhysRevApplied.21.L051001> for a detailed description of sample preparation, detection procedure, adiabatic approximation, and other experimental considerations including citation to Refs. [42,43].
- [21] C. S. Madasu, M. Hasan, K. D. Rathod, C. C. Kwong, and D. Wilkowski, Datta-das transistor for atomtronic circuits using artificial gauge fields, *Phys. Rev. Res.* **4**, 033180 (2022).
- [22] N. V. Vitanov, A. A. Rangelov, B. W. Shore, and K. Bergmann, Stimulated Raman adiabatic passage in physics, chemistry, and beyond, *Rev. Mod. Phys.* **89**, 015006 (2017).
- [23] H. Ammann and N. Christensen, Delta kick cooling: A new method for cooling atoms, *Phys. Rev. Lett.* **78**, 2088 (1997).
- [24] A. Valdés-Curiel, D. Trypogeorgos, Q.-Y. Liang, R. P. Anderson, and I. B. Spielman, Topological features without a lattice in Rashba spin-orbit coupled atoms, *Nat. Commun.* **12**, 593 (2021).
- [25] F. Leroux, K. Pandey, R. Rehbi, F. Chevy, C. Miniatura, B. Grémaud, and D. Wilkowski, Non-Abelian adiabatic geometric transformations in a cold strontium gas, *Nat. Commun.* **9**, 3580 (2018).
- [26] J. Ruseckas, G. Juzeliūnas, P. Öhberg, and M. Fleischhauer, Non-Abelian gauge potentials for ultracold atoms with degenerate dark states, *Phys. Rev. Lett.* **95**, 010404 (2005).
- [27] J. Y. Vaishnav, J. Ruseckas, C. W. Clark, and G. Juzeliūnas, Spin field effect transistors with ultracold atoms, *Phys. Rev. Lett.* **101**, 265302 (2008).
- [28] P. Kubala, J. Zakrzewski, and M. Łacki, Optical lattice for a tripodlike atomic level structure, *Phys. Rev. A* **104**, 053312 (2021).
- [29] T.-C. Tsui, Y. Wang, S. Subhankar, J. V. Porto, and S. L. Rolston, Realization of a stroboscopic optical lattice for cold atoms with subwavelength spacing, *Phys. Rev. A* **101**, 041603 (2020).
- [30] T. Frazer and K. Gillen, One-dimensional arrays of optical dark spot traps from nested Gaussian laser beams for quantum computing, *Appl. Phys. B* **128**, 90 (2022).
- [31] L. Amico *et al.*, Roadmap on atomtronics: State of the art and perspective, *AVS Quantum Sci.* **3**, 039201 (2021).
- [32] C. J. Bordé, C. Salomon, S. Avrillier, A. Van Lerberghe, C. Bréant, D. Bassi, and G. Scoles, Optical Ramsey fringes with traveling waves, *Phys. Rev. A* **30**, 1836 (1984).
- [33] C. J. Bordé, Atomic interferometry with internal state labelling, *Phys. Lett. A* **140**, 10 (1989).
- [34] M. Kasevich and S. Chu, Atomic interferometry using stimulated Raman transitions, *Phys. Rev. Lett.* **67**, 181 (1991).
- [35] R. H. Parker, C. Yu, W. Zhong, B. Estey, and H. Müller, Measurement of the fine-structure constant as a test of the standard model, *Science* **360**, 191 (2018).
- [36] L. Morel, Z. Yao, P. Cladé, and S. Guellati-Khélifa, Determination of the fine-structure constant with an accuracy of 81 parts per trillion, *Nature* **588**, 61 (2020).
- [37] V. Ménoret, P. Vermeulen, N. Le Moigne, S. Bonvalot, P. Bouyer, A. Landragin, and B. Desruelle, Gravity measurements below $10^{-9}g$ with a transportable absolute quantum gravimeter, *Sci. Rep.* **8**, 12300 (2018).
- [38] G. Rosi, F. Sorrentino, L. Cacciapuoti, M. Prevedelli, and G. Tino, Precision measurement of the Newtonian gravitational constant using cold atoms, *Nature* **510**, 518 (2014).
- [39] P. Asenbaum, C. Overstreet, M. Kim, J. Curti, and M. A. Kasevich, Atom-interferometric test of the equivalence principle at the 10^{-12} level, *Phys. Rev. Lett.* **125**, 191101 (2020).
- [40] Y.-X. Du, X.-X. Yue, Z.-T. Liang, J.-Z. Li, H. Yan, and S.-L. Zhu, Geometric atom interferometry with shortcuts to adiabaticity, *Phys. Rev. A* **95**, 043608 (2017).
- [41] K. Kotru, D. L. Butts, J. M. Kinast, and R. E. Stoner, Large-area atom interferometry with frequency-swept Raman adiabatic passage, *Phys. Rev. Lett.* **115**, 103001 (2015).
- [42] C. S. Madasu, *Experimental investigation of non-Abelian artificial gauge fields: from SU(2) to SU(3)*, Ph.D. thesis, Nanyang Technological University, 2023.
- [43] F. J. F. M. Leroux, *Non-Abelian Geometrical Quantum Gate Operation in an Ultracold Strontium Gas*, Ph.D. thesis, National University of Singapore, 2017.